Observations of reflectance distribution around sunglint from a coastal ocean platform

Wenying Su, Thomas P. Charlock, and Ken Rutledge

A scanning spectral photometer is deployed on a rigid coastal ocean platform to measure upwelling solar radiances from the sea surface at nine elevation angles spanning 150° of azimuth. Measured radiance distributions at 500 nm wavelength have been compared with traditional model simulations employing the Cox and Munk distribution of wave slopes. The model captures the general features of the observed angular reflectance distributions, but: (a) the observed peak value of sunglint near the specular direction is larger than simulated, except for a very calm sea; the model–measurement differences increase with wind speed and are largest for low solar elevation; (b) the observed sunglint is wider than simulated. In contrast to some previous studies, our results do not show a clear dependence of the mean square sea-surface slope on stability (air–sea temperature difference).

OCIS codes: 010.4450, 030.5620, 120.6200.

1. Introduction

If the sea surface were perfectly flat, a single, disklike reflected image of the Sun would be seen at the specular reflection angle. But this is almost never seen in reality. The sea surface is always rough due to the wind, and this spreads out the image of the Sun from a disk to the speckly column we are all familiar with. The principal effect of the rough surface is to reflect the direct solar beam into a range of angles; the rougher the sea, the wider the range.

Spooner[1] reported maximum slopes of 25° of measurements in the Tyrrhenina Sea, but he did not mention wind speed. Hulburt[2] observed maximum slopes in the North Atlantic increased from 15° at a wind speed of 2 m/s to 25° at a wind speed of 9 m/s. Shuleikin[3] took a long series of measurements over the Black Sea and deduced that slopes up to 30° were not uncommon.

W. Su is with the Center for Atmospheric Sciences, Hampton University, Hampton, Virginia 23668. T. P. Charlock is with the National Aeronautics and Space Administration Langley Research Center, 21 Langley Boulevard, Hampton, Virginia 23681. K. Rutledge is with Analytical Services & Materials, Inc., 107 Research Drive, Hampton, Virginia 23666.

Received 31 May 2002; revised manuscript received 9 September 2002.

0003-6935/02/357369-15$15.00/0

A. Cox and Munk

Cox and Munk[4,5] pointed out that the width of the glint pattern is an indication of the maximum slope of the sea surface. This is the basis of their technique to measure sea surface slope distribution by using photographs of sunglint. Their measurements were made from an airplane at an altitude of ~610 meters near the island of Maui. They related the density at each point in defocused versions of their sunglint photographs to the probability of occurrence for the wave slope corresponding to solar specular reflection. During the period of measurements the air–sea temperature differences were positive, namely neutral to positive stability.

Cox and Munk only took photographs for solar zenith angles (SZA) of less than 35°, partly because the Fresnel reflectance increases rapidly with SZA and thus the sunglint brightness can exceed the film's dynamic range. Also, this minimizes the shadowing problem. But taking data only at small SZA might cause bias in their derived mean square slope.

The measured parameters used to describe the sea slope distribution include mean square slope, skewness, and peakedness (also called kurtosis). Skewness corresponds to the most probable tilt a few degrees with the azimuth of ascent pointing downwind for low slopes and pointing upwind for very large slopes at higher wind speed. Peakedness corresponds to the probabilities of very large and very small slopes.

B. Recent Observations

After the classical work of Cox and Munk, no slope measurements were reported until 1970s. Since then, four main approaches are used for slope measurements: laser slope gauge, laser glitter, radar backscattering, and microwave. An optical sensor can detect water wave slopes generated by arbitrarily short water waves up to the wavelength of reflected light, while microwave radar can only measure a part of the surface slopes up to the radar wavelength.

The laser slope gauge approach determines local slopes from the refraction of a laser beam as it passes from an immersed laser source through the water–air interface to a receiver above the water. Slope statistics measured by Hughes *et al.*[6] for positive stability (air temperature greater than sea temperature) are in good agreement with those of Cox and Munk, showing a similar linear wind speed dependence for the mean square slope and a weak wind speed dependence for skewness and peakedness. Tang and Shemdin's results[7] differed significantly from Cox and Munk, with some of their mean square slopes exceeding the Cox and Munk values by as much as a factor of three; they did not report air–sea temperature differences. Haimbach and Wu[8] found a linear relationship between wind speed and mean square slope similar to the Cox and Munk result. They suggested that significant deviations from Cox and Munk are related to stability, with positive stability suppressing ripples to produce smaller mean square slopes, and negative stability enhancing ripples to produce larger mean square slopes. Measurements by Hwang and Shemdin[9] indicated deviations from the linear dependence of the mean square slope on wind speed found by Cox and Munk. The deviations were correlated with stability. They showed a reduction in the mean square slope for stable conditions and a sharp increase in the mean square slope for unstable conditions.

Shaw and Churnside[10] used a laser-glint technique, where the laser source is above the water instead of below it, and found that the mean square slope increases with negative stability at roughly the same rate as it decreases with moderately positive stability. Their measurements also show weak linear correlations of skewness and peakedness with wind speed. They found that skewness is very weakly correlated with stability, whereas peakedness is much more strongly correlated and tends to increase with negative stability.

Another approach uses sea-surface radar backscatter to derive mean square slope.[11–14] Only the ocean waves whose wavelengths are significantly longer than the radar wavelength make contribution to the measured mean square slope. There has been a lot of interest in this subject because of the recent use of radar satellites to derive ocean surface wind speed. Liu *et al.*[13] found that Gram–Charlier distribution used by Cox and Munk is appropriate only over a small range of slopes. They derive a new probability distribution function (PDF) for gravity wave slopes. They point out that peakedness of slopes is generated by nonlinear wave–wave interactions in the range of gravity waves, and the skewness of slopes is generated by nonlinear coupling between the short waves and the underlying long waves. Liu *et al.*[14] provided mean square slopes of gravity-capillary waves for clean surface and of gravity waves for both clean and slick surface. They compared their mean square slopes with the observations of Cox and Munk for clean and slick surfaces and concluded that the mean square slopes of Cox and Munk are approximately correct within the range investigated.

The final approach uses microwave emission. Trokhimovski[15] analyzed polarimetric microwave measurements of the sea-surface brightness temperature at several viewing angles and frequencies to obtain the mean square slope for gravity-capillary waves. They found that the mean square slope is 10% larger than the Cox and Munk slope approximation, and no difference is found between stable and unstable air–sea temperature differences in the mean square slope normalized to the Cox and Munk model.

C. Models

The traditional model of sunglint, used in almost all radiative transfer models, basically convolves the Fresnel reflectivities with the slope distribution of Cox and Munk. Shadowing is generally ignored, as is the finite width (0.5°) of the Sun. Oddly, no one has actually tested whether this model agrees with observed radiance data for the sunglint region.

Many remote sensing retrieval algorithms also use the slope statistics of Cox and Munk to simulate the reflectance of the ocean surface.[16–21] Note surface shadowing effects[22] are included in the model of Chowdhary.[20,21] Since Cox and Munk derived their slope statistics from reflected sunlight, this is somewhat of a closed loop in which no new information is added. By contrast, some of the more recent slope measurements, mentioned above, directly provide a microscale description of the sea-surface roughness. Tests to determine whether or not these microscale descriptions provide a correct macroscale image around the sunglint region are rare. Morel *et al.*[23] compared measured and simulated upwelling fluxes, but they did not specifically study the sunglint region.

Several theorists have attempted to improve, or at least further develop, this traditional sunglint model. Preisendorfer and Mobley[24] modeled the glint pattern of a wind-roughened sea surface as a function of environmental lighting conditions and wind speed. The simulation allows for multiple reflections of rays by wave facets and for the possibility of the shadowing of one facet by another. They pointed out the extraordinarily large range in sea slopes that are associated with the tiny capillary waves (wavelength <1.73 cm). Thus, they focused on constructing capillary waves in their model, using the mean square slope given by Cox and Munk. Their method shows a small, very dense sunglint pattern for a wind speed

of 1 m/s; as the wind speed increases, the glint pattern becomes broader and less dense at its center. Their simulations show that at a wind speed of 1 m/s, most of the wave-facet normals are tilted less than 5° from the vertical, while tilts of 10° or more are rare. But at a wind speed of 20 m/s, the tilt of some capillary wave facets exceeds 30°!

D. Remote Sensing

Accurate observing near the sunglint requires a sensor with a stable response over a huge dynamical range. Hence the glint region is usually avoided for remote sensing. For example, sea-viewing wide field-of-view sensor (SeaWiFS) has the operational capability of tilting the sensor 20° away from nadir to minimize sunglint contamination. Glint is still a factor near the subsolar point.[25] But some recent studies exploit the sunglint, because it essentially provides a bright source at the surface and because transmission measurements are relatively simple to interpret. Kleidman *et al*.[26] used the high reflection from sunglint to retrieve precipitable water vapor in the near infrared. The MODIS (moderate resolution imaging spectroradiometer)-Atmosphere group is developing a retrieval algorithm for aerosol absorption based on reflection from sunglint.[27] Whether we try to avoid sunglint contamination or try to exploit it, knowledge of the distribution of the reflection from the sunglint region is essential.

In this paper, we compare new measurements of sunglint from a coastal ocean platform with simulations by a radiative transfer model that uses the Cox and Munk slope distribution. Section 2 reviews the slope distribution of ocean waves. Section 3 introduces our measurements at the CERES (Clouds and the Earth's Radiant Energy System) (California environmental resources evaluation system) Ocean Validation Experiment (COVE) site. Section 4 describes the model simulations that are compared with measurements. Section 5 presents the results. Discussions and conclusions are in Sections 6 and 7.

2. Slope Distribution

Cox and Munk's results show that while the slope distribution of ocean waves is close to Gaussian, it is sufficiently different that a more complicated functional form is required. They fitted the data with a Gram–Charlier expansion:

$$p(x) = p_0(x)\left[1 + \sum_{n=1}^{N} \frac{c_n}{n!} H_n(x)\right], \tag{1}$$

where $p_0(x)$ is the closest Gaussian to $p(x)$. The $H_n(x)$ are Hermite polynomials. The size of the coefficients $\{c_n\}$ determines the deviation from the pure Gaussian case. The odd coefficients describe a skewness property for the PDF. The even coefficients define a property which is often called "peakedness", in that it may cause $p(x)$ to be more peaked than a pure Gaussian. Cox and Munk described the PDF of slopes by a two-dimensional Gram–Charlier distribution with two skewness coefficients and three peakedness coefficients:

$$\begin{aligned} p = (2\pi\sigma_c\sigma_u)^{-1} \exp\left[-\frac{1}{2}(\xi^2 + \eta^2)\right]\Bigg\{1 - \frac{1}{2}c_{21} \\ \times (\xi^2 - 1)\eta - \frac{1}{6}c_{03}(\eta^3 - 3\eta) + \frac{1}{24}c_{40}(\xi^4 - 6\xi^2 \\ + 3) + \frac{1}{4}c_{22}(\xi^2 - 1)(\eta^2 - 1) + \frac{1}{24}c_{04}(\eta^4 - 6\eta^2 \\ + 3)\Bigg\}, \end{aligned} \tag{2}$$

σ_c, σ_u are the crosswind (c) and upwind (u) root mean square slope components. ξ and η are normalized x and y slopes defined as

$$\xi = \frac{z_x}{\sigma_c}, \qquad \eta = \frac{z_y}{\sigma_u},$$

in which z_x and z_y are the crosswind and upwind components of the slope. The fit Eq. (2) is only valid within 2.5 standard deviations, i.e., $|\xi| < 2.5$ and $|\eta| < 2.5$.

In a famous formula Cox and Munk (cm in equations) fitted the total mean square slope as a function of wind speed:

$$\sigma_{\mathrm{cm}}{}^2 = \sigma_c{}^2 + \sigma_u{}^2 = 0.003 + 5.12 \times 10^{-3}U, \tag{3}$$

where U is the wind speed in m/s. The skewness coefficients are

$$c_{21} = 0.01 - 0.0086U, \qquad c_{03} = 0.04 - 0.033U \tag{4}$$

and the peakedness coefficients are

$$c_{40} = 0.40, \qquad c_{22} = 0.12, \qquad c_{04} = 0.23. \tag{5}$$

The important results from Cox and Munk's measurements are

1. The sea-slope probability distribution is approximately Gaussian.
2. The mean square slope increases linearly with wind speed; at a wind speed of 14 m/s, the slope is approximately 16°.
3. The distribution of the up/downwind component sea-surface slopes is skewed from Gaussian; the skewness increases with wind speed.
4. The peakedness, which is barely above the limit of observational error, shows no significant variation with wind speed.
5. The ratio, σ_u/σ_c, of the upwind to the crosswind component of mean square slope ranges from 1.0 to 1.9;
6. The primary axis of the 2D slope distribution [Eq. (2)] is closely aligned with the wind direction (indicating that capillary and short-wavelength locally-induced gravity waves are the main contributors to sunglint);

7. Oil slicks, which tend to suppress the capillary waves that are steeper, reduce the mean square slope by a factor of 2–3; they reduce skewness but leave peakedness unchanged.

Wu[28] reanalyzed the data of Cox and Munk, fitting the total mean square slope σ_{wu}^2 versus wind-speed data by using a two-branch logarithmic fit:

$$\begin{aligned}\sigma_{wu}^2 &= (\ln U + 1.2)10^{-2} && U \le 7 \text{ m/s} \\ &= (0.85\ln U - 1.45)10^{-1} && U > 7 \text{ m/s}, \end{aligned} \quad (6)$$

$\sigma_{wu}^2 < \sigma_{cm}^2$ for wind speeds less than 1 m/s, with differences of about 10%. For wind speeds between 1 and 5 m/s, $\sigma_{wu}^2 > \sigma_{cm}^2$, and the differences are up to 50%. For wind speeds between 5 and 11 m/s, $\sigma_{wu}^2 < \sigma_{cm}^2$, and the largest difference is 36%. For wind speeds larger than 11 m/s, $\sigma_{wu}^2 > \sigma_{cm}^2$, with differences of approximately 5 ~ 6%. By use of different analysis methods, the resulting mean square slopes can differ as much as 50%.

Shaw and Churnside[10] related mean square slope with stability. They normalized their mean square slope σ_{sc}^2 by σ_{cm}^2 and found:

$$\begin{aligned}\sigma_{sc}^2/\sigma_{cm}^2 &= 1.42 - 2.80Ri && -0.23 < \text{Ri} < 0.27, \\ \sigma_{sc}^2/\sigma_{cm}^2 &= 0.65 && \text{Ri} \ge 0.27, \end{aligned} \quad (7)$$

where the Richardson number, Ri, used to represent stability:

$$\text{Ri} = g\,\frac{\Delta T_{a-w}}{T_w U_z^2}. \quad (8)$$

Here g is the gravitational acceleration (9.8 m/s^2), ΔT_{a-w} is the air–sea temperature difference, U_z is the mean wind speed measured at height z (10 m), and T_w is the mean water temperature. Ri is positive for stable conditions (air warmer than water), zero for neutral cases (equal air and water temperature), and negative for unstable cases (air colder than water). When Ri = 0.15, σ_{sc}^2 equals σ_{cm}^2.

3. Measurements at COVE

The COVE site is a rigid ocean platform (owned by the US Coastguard) located 25 km off the coast of Virginia Beach at the mouth of the Chesapeake Bay. The platform rises 35 m from the ocean surface. The sea is 11 m deep at the site. Instruments at COVE include uplooking and downlooking pyranometers and pyrgeometers, a pyrheliometer on a solar tracker, and a Multi-Filter [sic] Rotating Shadowband Radiometer (MFRSR). The broadband observations subscribe to the rigorous protocols of the World Meteorological Organization's baseline surface radiation network (BSRN). COVE is an official aerosol network (AERONET) station equipped with a CIMEL Sun photometer. COVE is also a site for the ground-based GPS (global positioning system) integrated precipitable water vapor demonstration network. Meteorological measurements at COVE include temperature, relative humidity, pressure, wind speed, and wind direction. COVE is a NOAA (National Oceanic and Atmospheric Administration) National Data Buoy Center observation platform site and also provides measurements of wave height, dominant wave period, average wave period, swell height, large scale wave steepness, and water temperature.

Table 1. Viewing Distances from Nadir and Diameters of the Field of View of SP1A for Different Elevation Angles

Elevation Angle	Distance (m)	Diameter (m)
2	663.35	265.58
12	108.98	8.98
22	57.33	2.82
32	37.07	1.42
42	25.73	0.89
52	18.10	0.65
62	12.32	0.52
72	7.53	0.45
90	0.00	0.40

We use an SP1A Schulz spectral photometer to measure the upwelling radiance from the sea surface. It has 18 channels between 350 and 1050 nm, a fixed field of view of 1°, and is stable and accurate over the huge dynamical range characteristic of sunglint. It is mounted on a seaworthy Sagebrush tracker and scans the sea surface horizontally at nine elevation angles (2, 12, 22, 32, 42, 52, 62, 72, and 90 deg. These elevation angles are negative. For simplicity we omit the negative signs). For each elevation angle, it scans about 150° of azimuth (from 85 due north to 235 due north, 85N to 235N) and samples at intervals of 2.5°. The detector responds almost instantaneously. Each complete set of scanning measurements takes about 4.5 min, short enough that Sun angle variation is not a significant factor. The SP1A starts a new scan every 5 min. It is mounted 23 m from the sea surface on the edge of the platform. Table 1 lists the distances from nadir and the view diameters at the sea surface for each elevation angle. In this paper we only present results from the 500 nm wavelength channel. We used COVE data from four clear days: January 6, 10, 11, and 13, 2001.

4. Simulation

For simulating the radiances observed by the SP1A, we chose the widely used the second simulation of satellite signal in the solar spectrum (6S) model,[29] which employs the Cox and Munk distribution of wave slopes to parameterize the effect of wind on reflection by the sea. 6S does not simulate the effects of shadowing and air–sea temperature differences (stability) on radiance. 6S uses the successive order of scattering (SOS) method to compute the scattering properties of the aerosol and Rayleigh system, and 6S does not take account for polarization. Comparison between the scalar SOS results versus the vector SOS results shows that the error is small, which justifies the use of the scalar code when molecules and aerosols are mixed. But when Rayleigh scattering only is considered, polarization is taken

into account through empirically adjusted coefficients. 6S assumes the Sun is a point source.

The input data needed for 6S include wind speed and direction, aerosol optical depth (AOD) at 550 nm and ocean pigment concentration. AERONET Level 1.5 real-time cloud screened daily averaged AOD at 500 and 670 nm were linearly interpolated to 550 nm, yielding AOD values of 0.056, 0.033, 0.036, and 0.150 for the respective dates of Jan. 6, 10, 11, and 13. Pigment concentrations are from the SeaWiFS satellite. Wind speed and direction are measured once a minute at COVE from a height of 38 m by the *RM*-Young Wind Monitor. When using the Cox and Munk statistics, the wind must be scaled to 10 m; we use the following equation for this purpose[30]:

$$U = \frac{u_*}{k} \ln\left(\frac{z}{z_0}\right), \tag{9}$$

where u_* is friction velocity; z_0 is aerodynamic roughness length; and k is Von Karman constant. For this coastal site, we assume a value of 0.0009 for z_0.[30] The wind speed at 38 m is approximately 1.14 times of that at 10 m.

As the angle of elevation approaches the nadir, the instrument views only a $\sim$ 0.5 m area of the sea surface (Table 1), and the temporal signature of ocean capillary-gravity waves then becomes conspicuous. To smooth the influence of transient wave facets on the radiance distribution, measured radiances have been averaged over 30 min. In addition, azimuthally we apply seven points weighting average to all measured and simulated radiances/reflectances.

6S was used to simulate the radiance every 5 min, the same as the SP1A measurement sequence. The wind data were averaged every 5 min as input. 6S used the same viewing geometry and grid as the SP1A. Simulated 6S results were then averaged half hourly to compare with measurements. We normalize both the simulated and observed radiances to the solar irradiance at the top of the atmosphere and express them in terms of reflectance as

$$\rho(\theta_s, \theta_v, \Delta\varphi) = \frac{\pi L(\theta_s, \theta_v, \Delta\varphi) d^2}{\cos(\theta_s) E_{s0} {d_0}^2}, \tag{10}$$

where L is the radiance, E_{s0} is the extraterrestrial solar irradiance perpendicular to a plane surface at the mean Sun–Earth distance of d_0 and d is the Sun–Earth distance at the time of the measurement, θ_v is the viewing zenith angle, θ_s is the solar zenith angle, and $\Delta\varphi$ is the relative azimuth angle.

We now use the 6S model to see how sensitive the reflectance near the specular direction is to mean square slope (σ^2), peakedness coefficients, wind speed, and SZA. At each SZA (58°, 68°, 78°, which are the angles for our observations) in Figs. 1–3, we show the azimuthal distribution of specular reflectance (view elevations 32°, 22°, 12°) at different wind speeds. Figures 1–3 show that the simulation meets our intuitive expectations: peak specular reflectance decreases with wind speed (because reflection is diffused to a wider range of angle). Assuming Fresnel reflection for distributions of sea slopes defined by Eqs. (2)–(5), we obtained the solid curves in Figs. 1–4 Curves that are not solid represent perturbations of the mean square slopes (Fig. 1–3), and peakedness coefficients (Fig. 4) from the values assumed by Cox and Munk. Table 2 lists the ratios of specular reflectance calculated with mean square slope ${\sigma_{cm}}^2$ to specular reflectance calculated with doubling and halving ${\sigma_{cm}}^2$ for the three SZAs. At SZA of 58° and 68° doubling mean square slopes decreases maximum reflectance at the specular direction; halving mean square slopes increases maximum reflectance at the specular direction. At SZA of 78°, the impact of changes in mean square slopes to specular reflectance is even more highly dependent on wind speeds. For SZAs of 58° and 68°, and for the wind speeds of the domain of our observations (3.7–8.1 m/s for SZA 68° and 0.6–8.3 m/s for SZA 58°), the simulated maximum reflectances at the specular direction are in reverse proportion to the mean square slopes, and the ratios differ. Sensitivity studies were also carried out for peakedness coefficients at different SZAs and wind speeds. Increasing (decreasing) sea slope peakedness coefficients by a factor of 2, the maximum reflectance at the specular point increases (decreases) about 10% (5%) for different SZAs and wind speeds. Fig. 4 shows the results for SZA of 58° for wind speeds of 0.5, 5, and 12 m/s. The skewness coefficients have negligible impacts on the reflectance distributions of 6S (not shown).

5. Results

A. Comparison of Measurements with Simulations

For all four days of measurement, the sunglint was in the scanning range of the SP1A from 8 to 14 Local Standard Time (LST). Figure 5 shows 30 min mean measured and simulated reflectances for 0800–0830 LST for Jan. 6 with view elevation angles from 2° to 72° and view azimuth angles from 85° to 235°. The mean effective SZA is 83.1°; and the mean solar azimuth angle (SAA) is 124.7°. The mean wind speed (direction) for the 30 min interval is 5.8 m/s (251.4 °N). While the measured sunglint pattern resembles the simulation, the measured reflectance near the peak of the glint is greater than the simulation; and the measured sun glint extends to a larger range in azimuth. The simulated reflectance in the sunglint region near the horizon is smaller than what we observed.

Figure 6 is similar to Fig. 5, but later on the same day with a higher Sun. It shows the measured and simulated reflectances at 12 LST for SZA of 59.3° and SAA of 178.0°. The mean wind speed (direction) for the 30 min interval is 4.9 m/s (244.5 °N). As at 8 LST, general features of the measured reflectance distribution are in good agreement with the simulations. But again, measured reflectance around the peak of the sunglint is more intense and covers a larger region than what 6S predicted. For this SZA of 59.3°, a flat sea would produce specular reflection

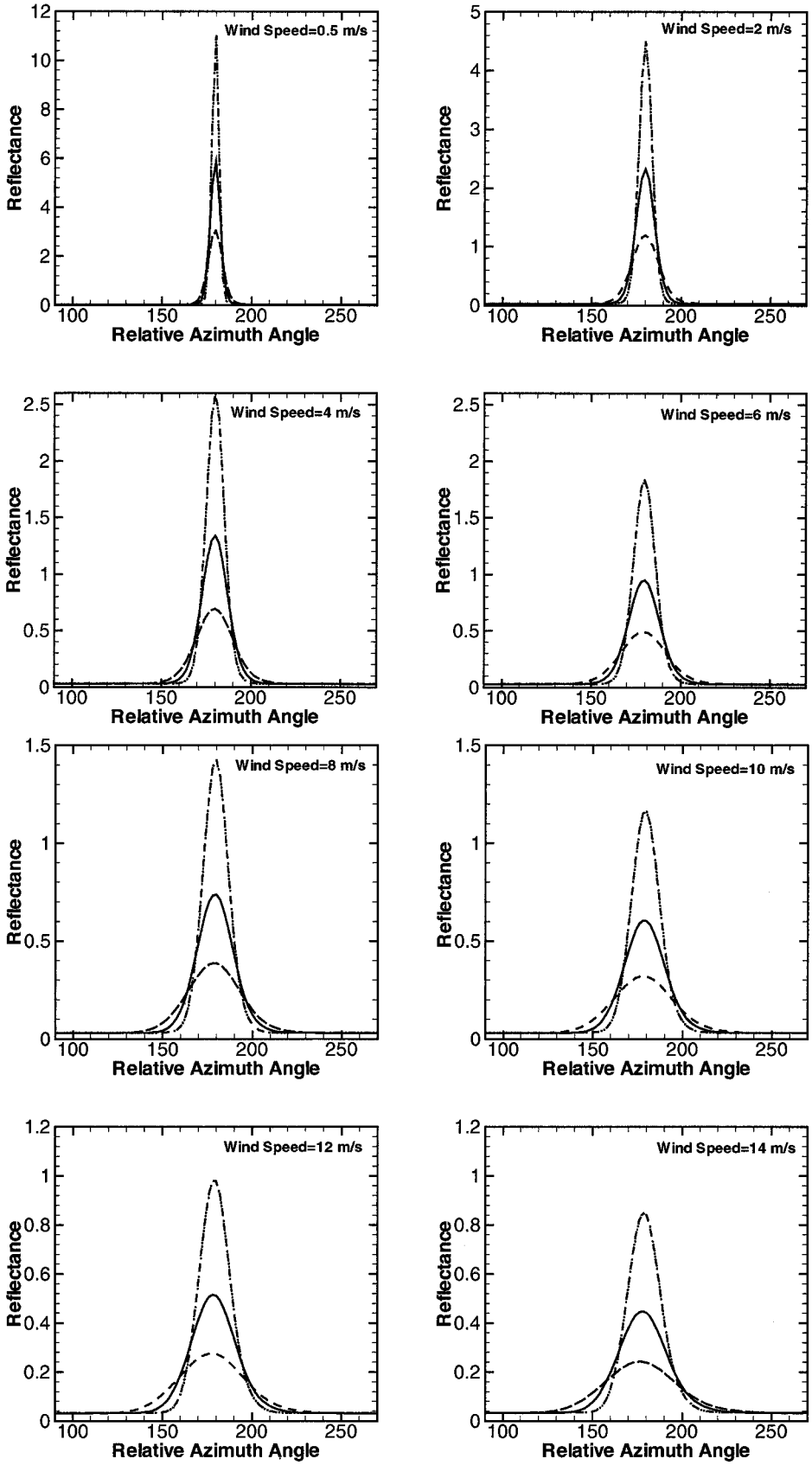

Fig. 1. Azimuthal reflectance distributions for solar zenith angle of 58° for different wind speeds and mean square slope (solid curve: σ_{cm}^2, dashed curve: $\sigma_{cm}^{2*}2$, dashed-dotted curve: $\sigma_{cm}^2/2$).

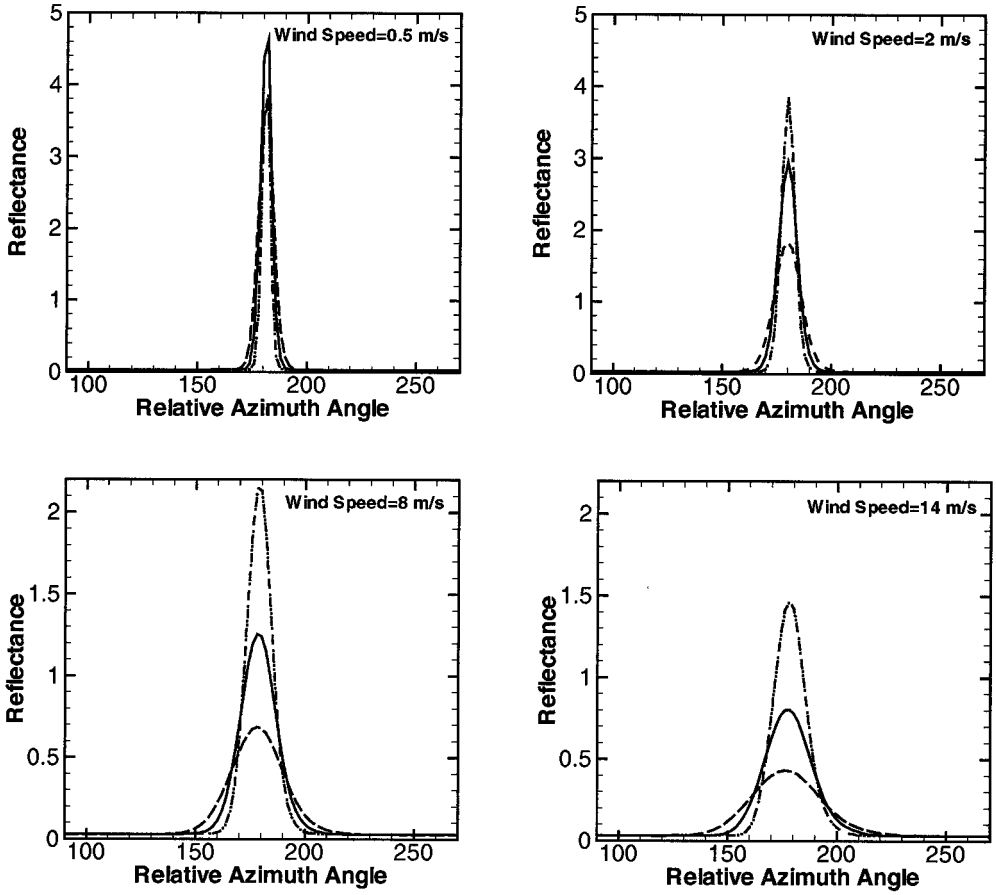

Fig. 2. Azimuthal reflectance distributions for solar zenith angle of 68°. Other parameters the same as for Fig. 1.

at a view elevation of 30.7°. While the distribution of facets in 6S produces a peak reflection well below 30.7 [Fig. 6(b)], the observed peak is much closer to the horizon [Fig. 6(a)].

The mean and maximum reflectance at 12 LST is smaller than at 08 LST, as expected, because reflectance decreases as SZA decreases. However, a larger region of the sea has significant sunglint (reflectance greater than 0.2) than at 08 LST (Fig. 5).

Figure 7 shows the differences between the observed reflectance and the simulated reflectance for 08 LST and 12 LST. Besides the fact that measured reflectance around the sunglint is more intense and covers a larger region than what 6S predicted, it is very obvious that the observed maximum reflectances shift to the horizon.

B. RM: Ratio of Observed Maximum Reflectance to Simulated Maximum Reflectance

Figure 8 shows the observed and simulated reflectances as a function of viewing azimuth angle for the specular viewing zenith angle only (the maximum glint is often at a different angle than the specular viewing zenith angle). Figures 8(a) and 8(b) show that the measured reflectances around the sunglint are larger than simulated, and the measured glint covers a larger range of azimuth. Fig. 8(a) shows the half-hour-averaged reflectances at a view elevation angle of 12° when the half hourly mean SZA is approximately 78.4°. Figure 8(b) is for the view elevation angle of 32° when half hourly mean SZA is 59.3°. The vertical scales in Figs. 8(a) and 8(b) differ by a factor of 7 due to the much higher maximum reflectance for low Sun (large SZA). At low Sun [Fig. 8(a)], the glint at the elevation of the specular direction spans a smaller range of azimuth than at high Sun [Fig. 8(b)]. We can thus summarize the glint distribution as thin and tall for low Sun and fat and short for high Sun.

As peak reflectance differs by approximately an order of magnitude with SZA, a normalization of glint reflectance would be convenient. To normalize, we first determine the largest reflectance, either observed or simulated. We then divide the observed reflectance by this maximum value. And we divide the simulated reflectance by the same maximum value. This is done for each elevation angle. The normalization process can be summarized as

$$R_{\max} = \max(R_{\text{obs}}, R_{\text{sim}}),$$

$$R_{n\_\text{obs}} = \frac{R_{\text{obs}}}{R_{\max}},$$

$$R_{n\_\text{sim}} = \frac{R_{\text{sim}}}{R_{\max}},$$

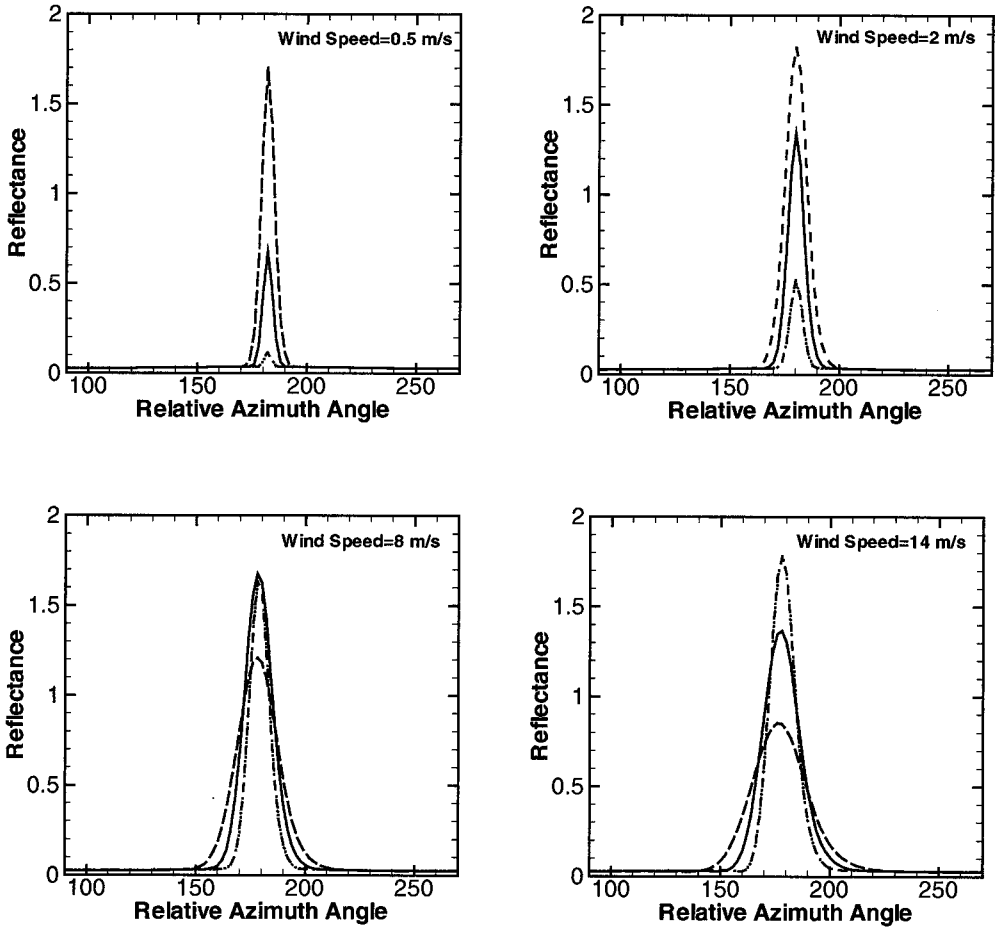

Fig. 3. Azimuthal reflectance distributions for solar zenith angle of 78°. Other parameters the same as for Fig. 1.

where R_{obs}, R_{sim} are observed and simulated reflectances; R_{n_obs}, R_{n_sim} are normalized observed and simulated reflectances. The normalized reflectance was then in the range of 0 to 1.

Define *RM* as the ratio of observed maximum reflectance to simulated maximum reflectance at the specular viewing zenith angle. Model simulations with the slope distribution of Cox and Munk show that the maximum reflectance is determined mainly by the mean square slope (Figs. 1–3), with only minor influence by the peakedness (Fig. 4). As Cox and Munk indicate that mean square slope depends on wind speed [Eq. (3)] while peakedness is independent of wind speed [Eq. (5)], *RM* can then be used as an indicator of the deviation of the real mean square slope from the one given by Cox and Munk. Table 3 gives, for elevation angles of 12°, 22°, and 32°, the half-hour mean wind speeds (m/s), maximum reflectances R_{max}, *RM*, and mean *RM* for each wind speed group. At elevation angle of 12° (first panel of Table 3) model simulations underestimate the peak reflectance by roughly a factor of 2 for wind speeds of 3.7–6.7 m/s and up to 3.3 at wind speed of 7.1 m/s. At an elevation angle of 22° (second panel of Table 3) observed peak reflectances are 1.28, 1.40, and 2.12 times larger than simulated for wind speeds of 3–4 m/s, 5–6 m/s, and 7–8 m/s. At an elevation angle of 32° (third panel of Table 3), the data covers a larger range of wind speed (from 0.6 to 8.3 m/s). At a very low wind speed, say less than 1 m/s, the *RM* is 0.76, which means that the observed peak reflectance is now less than simulated. For wind speeds of 1–2 m/s, 4 m/s, 5–6 m/s, and 7–8 m/s, the average *RM* values at elevation angle 32° are 1.17, 1.13, 1.22, and 1.42, respectively. It is clear that at each elevation angle, *RM* increases with wind speed. And *RM* decreases as view elevation angle increases. For a very calm ocean surface, with a wind speed of less than 1 m/s, the 6S simulation overestimates the peak reflectance; and for wind speeds larger than 1 m/s, it underestimates the peak reflectance.

Figure 9 shows the linear regression relationships between *RM* and wind speed for three elevation angles. The correlation coefficients are 0.49, 0.58, and 0.67 for elevation angles of 12°, 22°, and 32° (for which SZAs differ). This is not statistically significant except marginally for the third case. The regression relationship for 12° [Fig. 9(a)], which is quite different from the other two, indicates a larger deviation from the reflectance predicted by using σ_{cm}^2. Note that at an elevation angle of 12°, $RM > 1$ for wind speeds ranging from 3.7 to 7.1 m/s. Sensitivity studies show that for this wind speed range (Fig. 3), maximum theoretical reflectance occurs approxi-

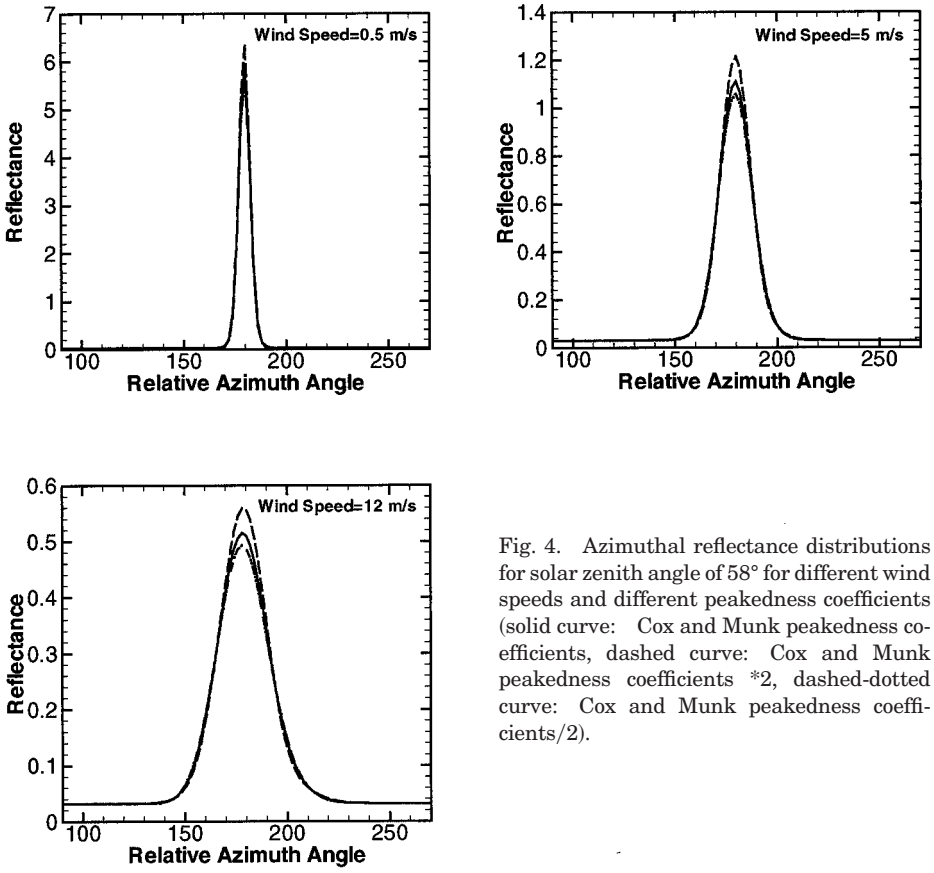

Fig. 4. Azimuthal reflectance distributions for solar zenith angle of 58° for different wind speeds and different peakedness coefficients (solid curve: Cox and Munk peakedness coefficients, dashed curve: Cox and Munk peakedness coefficients *2, dashed-dotted curve: Cox and Munk peakedness coefficients/2).

mately at the mean square slopes given by Cox and Munk. If the actual mean square slope (σ^2) is substantially less than or greater than σ_{cm}^2, basic theory indicates that reflectances will then be less than those of Cox and Munk at the specular angle. It is thus difficult to explain why $RM > 1$ for an elevation angle of 12° for wind speeds from 3.7 to 7.1 m/s: $RM > 1$ means the observed maximum reflectance is greater than the simulated maximum of Cox and Munk. At elevation angles of 22° and 32° for wind speeds greater than 1 m/s, $RM > 1$, which means we can decrease σ_{cm}^2 to account for the increase of the maximum reflectance at the specular angle. Apparently for the same slope distribution, different illumination conditions produce different reflectance distributions.

Figure 10 shows observed reflectance distributions for Jan. 10 and 11 at 12:30 LST; wind speeds are 4.8 and 0.6 m/s, respectively. Because the illumination conditions and AODs are very similar for these two days, we expect that wind speed is the cause for the different reflectance distributions. When the sea is very calm, the sunglint covers a small region, and the largest reflectance is close to the specular direction [Fig. 10(b)]. As the wind speed increases, the sunglint covers a larger region, and the largest reflectance moves toward the horizon. This shift of the largest reflectance from specular point to horizon as wind speed increases was unexpected. A comparison of measurement and theory (Fig. 7) shows that the 6S code has not captured this feature. At 12:30 LST of Jan. 11 when wind speed is 0.6 m/s, the RM is less than 1 (the measured reflectance is smaller than simulated), while as wind speed increases, RM is greater than 1 (see Table 3). From the model sensitivity studies for this elevation and wind speed (Fig. 1), we infer that the maximum reflectance at the specular point varies inversely with σ^2. This implies that RM varies directly as σ_{cm}^2/σ^2. As data in

Table 2. Ratios of Specular Reflectance[a]

Wind Speed (m/s)	$\text{Ref}(\sigma_{cm}^2)/\text{Ref}(2\times\sigma_{cm}^2)$ Solar Zenith Angle			$\text{Ref}(\sigma_{cm}^2)/\text{Ref}(\sigma_{cm}^2/2)$ Solar Zenith Angle		
	58°	68°	78°	58°	68°	78°
0.5	1.93	1.25	0.40	0.53	0.83	5.67
2	1.95	1.60	0.74	0.52	0.76	2.58
4	1.94	1.73	1.05	0.52	0.65	1.61
6	1.94	1.80	1.24	0.52	0.61	1.23
8	1.90	1.82	1.42	0.52	0.58	1.06
10	1.88	1.86	1.46	0.52	0.57	0.87
12	1.85	1.88	1.55	0.52	0.56	0.82
14	1.88	1.86	1.59	0.53	0.55	0.78

[a]Calculated with mean square slope given by Cox and Munk σ_{cm}^2 to specular reflectance calculated with doubling and halving σ_{cm}^2.

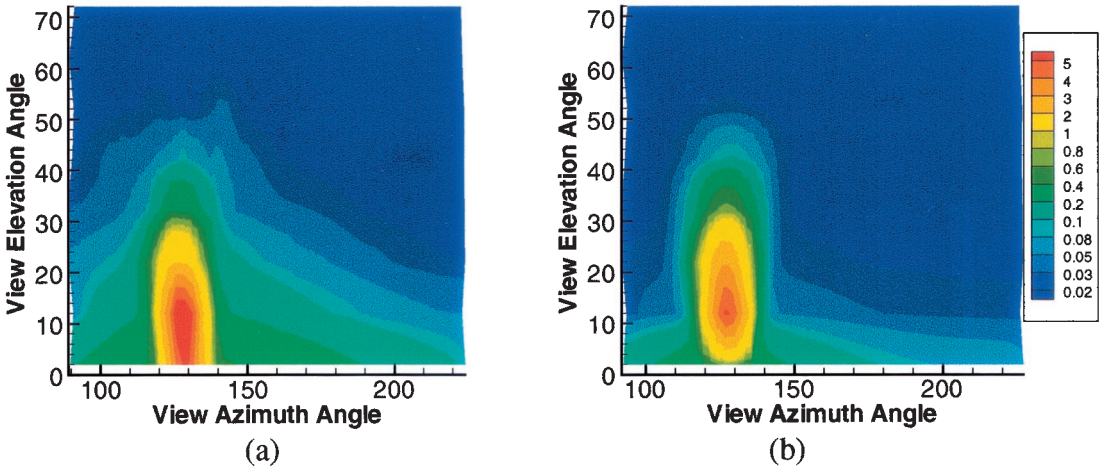

Fig. 5. (a) Measured and (b) simulated reflectances for Jan. 6 at 08 LST. SZA is 83.1. Wind speed is 5.8 m/s and wind direction is 251.4. AOD is 0.056.

Table 3 show $RM < 1$ ($RM > 1$) for wind speeds less (greater) than 1 m/s, we would further infer $\sigma_{cm}^2 < \sigma^2$ ($\sigma_{cm}^2 > \sigma^2$) from our observations for wind speed less (greater) than 1 m/s. This suggests that Eq. (3) should have a larger offset (than 0.003) and/or a smaller slope (than 5.12×10^{-3}) at very low wind speeds. But note that our observations and those of Cox and Munk are very sparse below 1 m/s.

C. Width of Sunglint

In Figs. 5, 6, and 8 the measured sunglint covers a larger range of azimuth than the simulated sunglint. We define the left-hand side (right-hand side) azimuth span of the sunglint as the absolute value of the difference, from a relative azimuth of 180° to where the normalized reflectance on the left-hand side (right-hand side) drops to 0.1. Adding the azimuth spans of the left-hand side and the right-hand side, we obtain the full width of the sunglint coverage. Figure 11 shows simulated azimuth width of sunglint versus observed. It is clear that the observed sun glint width is larger than the simulated width. Typical differences are 1 to 8 deg. The regression relationship between them is

$$\Delta\varphi_{sp} = 5.95 + 0.9787\Delta\varphi_{6s} \tag{11}$$

The correlation coefficient is 0.9324 and the root mean square is 3.037.

The asymmetry of the sea slope distribution was addressed as skewness in Cox and Munk. Skewness increases with wind speed. At higher wind speeds the most probable azimuth of ascent for small slopes is directed downwind, whereas for large slopes it is directed upwind. Because of the coarse azimuth resolution (2–3 deg.) of our sampling with SP1A, we cannot verify the skewness coefficients given by Cox and Munk.

D. Stability

We now use hourly NOAA data at COVE to investigate the effect of air–sea temperature differences

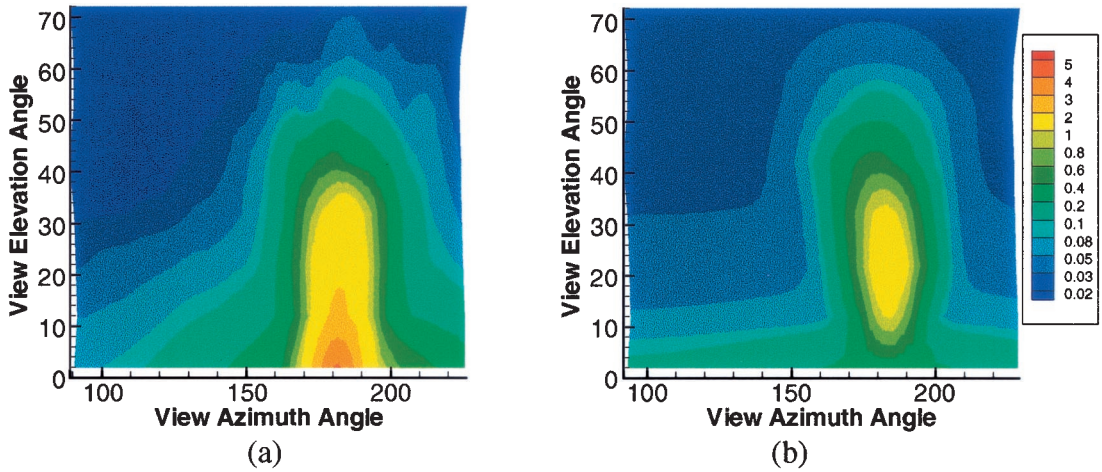

Fig. 6. (a) Measured and (b) simulated reflectances for Jan. 6 at 12 LST. SZA is 59.3. Wind speed is 4.9 m/s and wind direction is 244.5. AOD is 0.056.

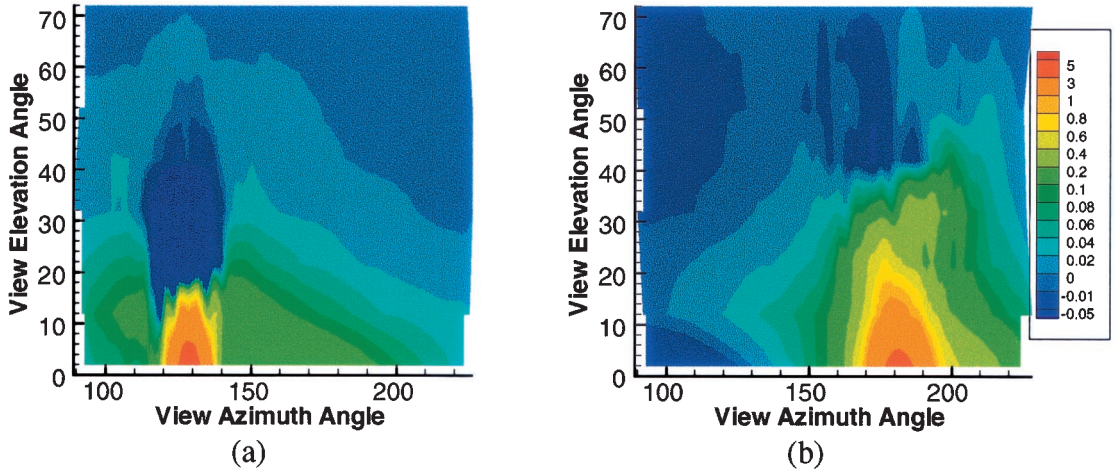

Fig. 7. Differences between the observed reflectance and the simulated reflectance for (a) 08 LST and (b) 12 LST.

(stability) on sea slopes and ocean optics. From the air–sea temperature differences, we see that only Jan. 11 is stable; Jan. 13 is nearly neutral; and Jan. 6 and 10 are unstable. According to Shaw and Churnside[10] when Ri is less than 0.15 [Eq. (7)], their measured σ_{sc} is larger than σ_{cm}. We anticipate that *RM*, the ratio of observed maximum reflectance to simulated maximum reflectance at the specular viewing zenith angle, will be strongly related to the difference of the real mean square sea slope σ^2 and σ_{cm}^2. Lacking actual small-scale sea slope measurements at COVE, we thus examine the relationship between *RM* and the Richardson number [Eq. (8)], using hourly data. Figure 12 is a scatter plot of *RM* and Ri. Maximum *RM* is found at neutral stability.

From the Shaw and Churnside[10] results for the relationship of real versus Cox and Munk sea slopes with Ri, we expect that $\sigma_{sc}^2 > \sigma_{cm}^2$ for $Ri < 0.15$, and $\sigma_{sc}^2 < \sigma_{cm}^2$ for $Ri > 0.15$. At SZAs of 58° and 68° and the wind speed range that we considered, the peak reflectance is in reverse proportion to σ^2, thus $RM \propto \sigma_{cm}^2/\sigma^2$. Interpreting Shaw and Churnside[10] for $Ri < 0$, we infer $RM < 1$. To the contrary, we find $RM > 1$ for all but the lowest wind speeds. Our results do not suggest a highly coherent relationship of σ^2/σ_{cm}^2 and Ri. Our data indicates that σ^2 is smaller than σ_{cm}^2 for both negative and positive stabilities with the maximum deviation at neutral stability except for very calm conditions.

6. Discussion

The peak values of our measured reflectances at the specular point are larger than those simulated, and the azimuth width of the glint is larger than simulated. For SZAs of 58° and 68° and wind speeds greater than 1 m/s, when σ_{cm}^2 increases (decreases), the peak value decreases (increases) but the azimuth width increases (decreases). By use of the same data as Cox and Munk but different analysis methods, Wu[28] found values of σ^2 differing from σ_{cm}^2 by a factor of 2. Reducing the σ_{cm}^2 value for SZAs of 58° and 68° would increase the maximum (peak) reflectance but would not increase the azimuth width. Can we reconcile theory and our data by increasing

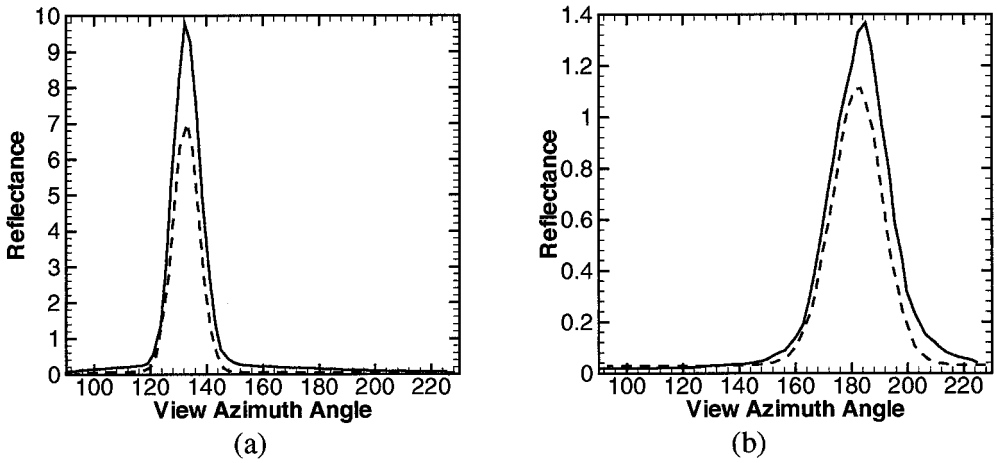

Fig. 8. (a) Azimuthal distribution of observed (solid curve) and simulated (dashed curve) reflectances for view elevation angle of 12° for 08:30 LST, Jan. 6, 2001 when SZA is approximately 78.4°, (b) for view elevation angle of 32° for 12:00 LST when SZA is 59.3°.

Table 3. Parameters for Three Elevation Angles

DOY-Time	SZA	Wind Speed	Maximum Reflectance	RM	Average RM
Elevation = 12					
11-1400	73.7	3.7	10.0	2.04	2.05
11-1330	78.2	4.8	13.1	2.06	
6-1330	78.4	5.1	9.78	1.40	2.12
6-1400	74.0	6.1	6.20	1.77	
10-1330	78.3	6.1	10.05	1.64	
10-1400	73.8	6.4	7.00	1.72	
13-1400	73.6	6.7	6.52	4.09	
13-1330	78.1	7.1	7.80	3.30	3.30
Elevation = 22					
10-1930	67.4	3.7	5.71	1.31	1.28
11-1430	69.7	4.0	4.33	1.25	
11-1530	63.2	4.0	2.77	1.29	
10-1900	64.2	4.6	4.49	1.25	
11-1500	66.1	5.4	2.88	1.49	1.40
6-1500	66.5	6.1	2.35	1.22	
6-1530	63.6	6.4	2.29	1.46	
6-1430	70.0	6.5	3.35	1.34	
10-1430	69.8	6.8	3.12	1.26	
10-1500	66.2	6.8	2.27	1.25	
10-1530	63.3	6.8	2.26	1.41	
13-1430	69.5	6.8	3.03	1.84	
13-1500	65.9	7.0	2.41	2.08	2.12
13-1930	66.8	7.2	3.73	2.02	
13-1900	63.7	7.5	4.36	2.59	
13-1530	62.9	8.1	1.75	1.78	
Elevation = 32					
11-1730	58.8	0.6	3.80	0.74	0.76
11-1800	59.8	0.8	3.16	0.78	
11-1830	61.6	1.6	2.95	1.29	1.17
11-1700	58.6	2.9	1.48	1.04	
6-1700	59.3	4.9	1.37	1.23	
11-1630	59.3	4.9	1.69	1.58	
6-1830	62.4	4.1	1.40	0.95	1.13
10-1800	59.9	4.6	1.39	0.88	
6-1800	60.6	4.6	1.55	1.16	
11-1600	60.9	4.6	1.48	1.29	
10-1730	58.9	4.8	1.16	0.96	
10-1700	58.8	4.9	1.13	1.02	
6-1730	59.5	5.0	1.05	0.99	1.22
6-1630	60.0	5.1	1.31	1.27	
6-1600	61.4	5.4	1.05	1.03	
10-1830	61.7	5.4	1.77	1.42	
10-1630	59.5	5.8	1.15	1.18	
13-1700	58.3	6.8	0.93	1.41	
13-1730	58.4	7.4	0.87	1.36	1.42
13-1630	59.0	7.8	0.81	1.37	
13-1800	59.4	8.2	1.19	1.69	
13-1830	61.2	8.2	1.04	1.44	
13-1600	60.6	8.3	0.74	1.25	

σ_{cm}^2 and thereby increase the azimuth width, while simultaneously increasing the peakedness coefficients to compensate for the reduction in maximum reflectance? Peakedness coefficients are constant in the results of Cox and Munk [Eq. (5)]. Could peakedness instead increase with wind speed and cause maximum reflectance to increase and match our SP1A observations? Simulations show that for SZAs of 58° and 68° and wind speeds greater than 1 m/s, increasing (decreasing) σ_{cm}^2 by a factor of 2 will decrease (increase) the maximum reflectance by factors between 1.6 and 1.9 (Table 2). But Fig. 4 shows that by increasing peakedness coefficients 2 (4) times, the maximum reflectance only increases 1.1 (1.3) times. Further, the azimuth width becomes smaller as peakedness coefficients increase to a certain point. This means a small change in σ_{cm}^2 would require a huge modification of the peakedness coefficients to produce the desired compensation. For example, at SZA of 58°, by doubling σ_{cm}^2 and at the same time increasing peakedness coefficients by 8 times, the simulated peak reflectance would not even return to its value as simulated with the original σ_{cm}^2 and peakedness. And increasing peakedness coefficients by factors larger than 4 would also reduce the azimuth width. Such manipulations of σ_{cm}^2 and the peakedness coefficients are unlikely to produce the azimuth distribution of reflectance that we observed.

For SZA of 78° and the wind speeds that we considered, sensitivity studies (Fig. 3) show that the maximum reflectance occurs very near the mean square slopes given by Cox and Munk. Smaller reflectances would be produced by either increases in σ_{cm}^2 or decreases in σ_{cm}^2. It is then difficult to explain why our *RM* is greater than 1 for an elevation angle of 12° (Table 3). Changing skewness coefficients by a factor of 2 in the model would hardly produce any discernible changes in the reflectance distributions. The discrepancy between the measured and simulated sunglint distribution indicates the need for revision (for studies at the present refined level) of the slope distribution given by Cox and Munk. We may need more terms in the Gram–Charlier expansion for skewness and peakedness, or a new analytical slope distribution function. Liu *et al.*[13] has already pointed out that the PDF of slopes within six times of the standard deviation cannot be described by the Gram–Charlier distribution given by Cox and Munk. Hence Liu *et al.*[13] derived a new PDF for large slopes.

7. Conclusions

We compared measured reflectance distributions for sunglint at the COVE site with simulations using the Cox and Munk slope distribution as parameterized by the 6S radiative transfer model. The measured sunglint shapes are generally in good agreement with the model simulations, but the measured reflectance is more intense and covers a larger region.

We define *RM* as the ratio of observed maximum reflectance to simulated maximum reflectance of the

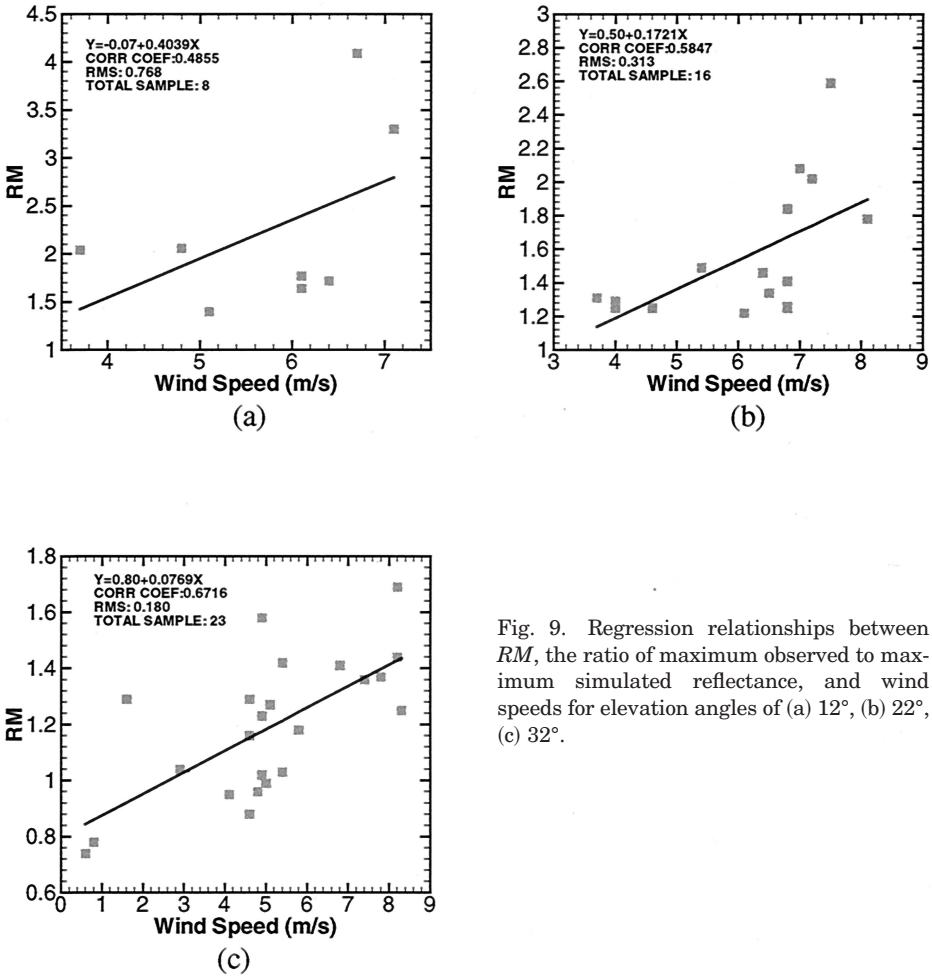

Fig. 9. Regression relationships between *RM*, the ratio of maximum observed to maximum simulated reflectance, and wind speeds for elevation angles of (a) 12°, (b) 22°, (c) 32°.

specular viewing zenith angle. Because at SZAs of 58° and 68°, the observed peak reflectance is in reverse proportion to σ^2 for wind speeds greater than 1 m/s, thus $RM \propto \sigma_{cm}{}^2/\sigma^2$. At a given view elevation angle, *RM* increases with wind speed. But *RM* decreases with increasing view elevation angle (decreasing SZA). *RM* is greater than 1, which means the real mean square slope is smaller than $\sigma_{cm}{}^2$, except for a wind speed of less than 1 m/s. At very low wind speed, the observed reflectance distribution is close to what the Fresnel equation predicted, with the largest reflectance happening near the specular

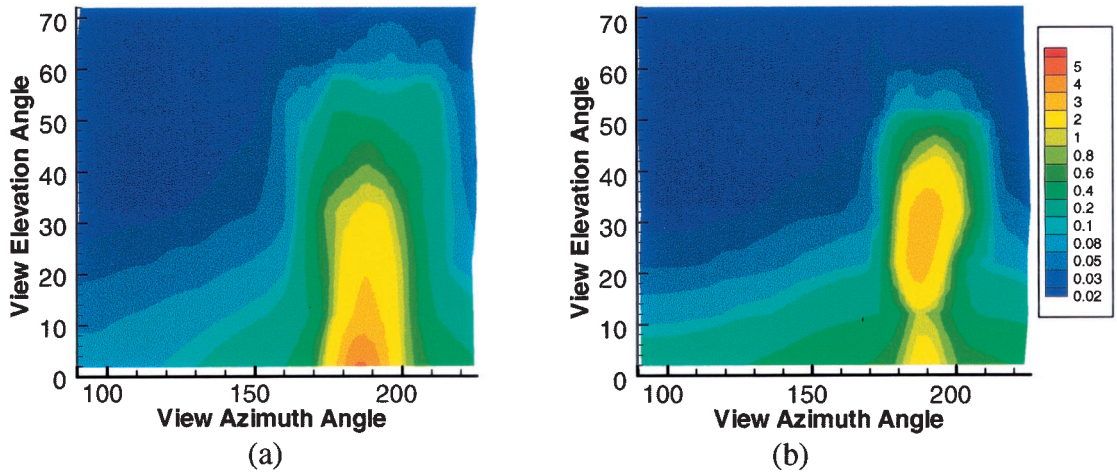

Fig. 10. Observed reflectance distributions for (a) Jan. 10 and (b) 11 at 12:30 LST, wind speeds are 4.8 (b) 0.6 m/s. AODs are 0.033 and 0.036.

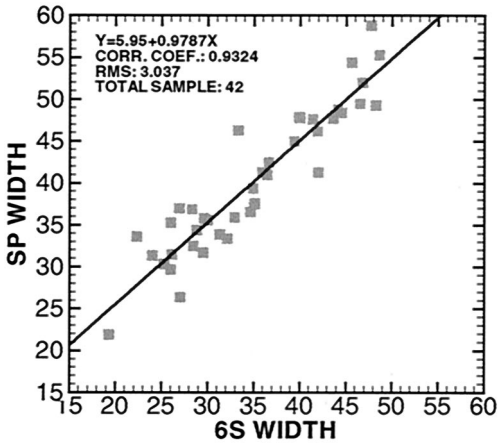

Fig. 11. Relationship between simulated and observed azimuth width of sunglint for January 6, 10, 11, and 13, 2001 at COVE.

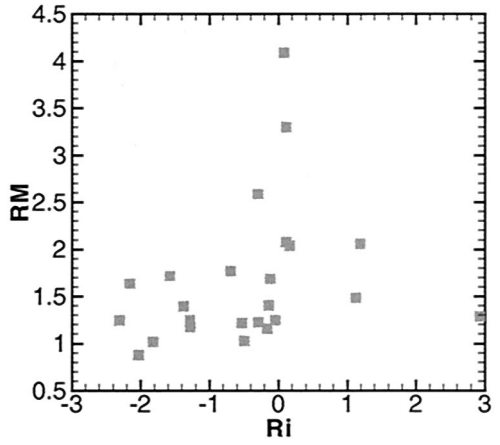

Fig. 12. Relationship between *RM* (the ratio of maximum observed to maximum simulated reflectance) and Ri (Richardson number).

point. As the wind speed increases, the largest reflectance shifts toward the horizon.

We calculated the width of the sunglint by measuring the azimuth span for normalized reflectance greater than 0.1 on each side of the specular point. The observed width is larger than the simulated width.

Our results do not suggest a dependence of mean square slope on stability. σ^2 is smaller than $\sigma_{cm}{}^2$ for both negative and positive stabilities, with the maximum deviation happening at neutral stability, except for very calm conditions.

COVE team members, K. Hoffmann and J. Madigan each provided software programming and operational support that contributed significantly to this research. W. Su's participation was funded by the NASA/GEWEX Global Aerosol Climatology Project (GACP). We acknowledge AERONET COVE PI B. Holben for providing Cimel aerosol optical thickness data.

References

1. J. Spooner, "Sur la lumiere des ondes de la mer," Corresp. Astronomique du Baron de Zach **6,** 331 (1822).
2. E. O. Hulburt, "The polarization of light at sea," J. Opt. Soc. Am. **24,** 35–42 (1934).
3. V. V. Shuleikin, *Fizika Moria* (*Physics of the Sea*), (Izv. Akad. Nauk., Moscow, USSR, 1941) p. 833.
4. C. Cox and W. Munk, "Measurement of the roughness of the sea surface from photographs of the sun's glitter," J. Opt. Soc. Am. **44,** 838–850 (1954).
5. C. Cox and W. Munk, "Statistics of the sea surface derived from sun glitter," J. Mar. Res. **13,** 198–227 (1954).
6. B. A. Hughes, H. L. Grant, and R. W. Chappell, "A fast response surface-wave slope meter and measured wind-wave moments," Deep-Sea Res. **24,** 1211–1223 (1977).
7. S. Tang and O. H. Shemdin, "Measurement of high frequency waves using a wave follower," J. Geophys. Res. **88,** C14, 9832–9840 (1983).
8. S. P. Haimbach and J. Wu, "Field trials of an optical scanner for studying sea-surface fine structures," IEEE J. Ocean. Eng. **OE-10,** 451–453 (1985).
9. P. A. Hwang and O. H. Shemdin, "The dependence of sea surface slope on atmospheric stability and swell conditions," J. Geophys. Res. **93,** C11, 13,903–13,912 (1988).
10. J. A. Shaw and J. H. Churnside, "Scanning-laser glint measurements of sea-surface slope statistics," Appl. Opt. **36,** 4202–4213 (1997).
11. Y. Liu and W. J. Pierson, "Comparisons of scatterometer models for the AMI on ERS-1: The possibility of systematic azimuth angel biases of wind speed and direction," IEEE Trans. Geosci. Remote Sens. **32,** 626–635 (1994).
12. Y. Liu and X.-H. Yan, "The wind-induced wave growth rate and the spectrum of the gravity-capillary waves," J. Phys. Oceanogr. **25,** 3196–3218 (1995).
13. Y. Liu, X.-H. Yan, W. T. Liu, and P. A. Hwang, "The probability density function of the ocean surface slopes and its effects on radar backscatter," J. Phys. Oceanogr. **27,** 782–797 (1997).
14. Y. Liu, M.-Y. Su, X.-H. Yan, and W. T. Liu, "The mean-square slope of ocean surfacewaves and its effects on radar backscatter," J. Atmos. Oceanic Tech. **17,** 1092–1105 (2000).
15. Y. G. Trokhimovski, "Gravity-capillary wave curvature spectrum and mean-square slope retrieved from microwave radiometric measurements (Coastal Ocean Probing Experiment)," J. Atmos. Oceanic Tech. **17,** 1259–1270 (2000).
16. M. I. Mishchenko and L. D. Travis, "Satellite retrieval of aerosol properties over the ocean using measurements of reflected sunlight: effect of instrumental errors and aerosol absorption," J. Geophys. Res. **102,** 13,543–13,553 (1997).
17. M. I. Mishchenko, I. V. Geogdzhayev, B. Cairns, W. B. Rossow, and A. A. Lacis, "Aerosol retrievals over the ocean by use of channels 1 and 2 AVHRR data: sensitivity analysis and preliminary results," Appl. Opt. **38,** 7325–7341 (1999).
18. P. Goloub, D. Tanre, J. L. Deuze, M. Herman, A. Marchand, and F. M. Breon, "Validation of the first algorithm applied for deriving the aerosol properties over the ocean using the POLDER/ASEOS measurements," IEEE Trans. Geosci. Remote Sensing **37,** 1586–1596 (1999).
19. J. L. Deuze, M. Herman, P. Goloub, D. Tanre, and A. Marchand, "Characterization of aerosols over ocean from POLDER/ADEOS-1," Geophys. Res. Lett. **26,** 1421–1424 (1999).
20. J. Chowdhary, B. Cairns, M. Mishchenko, and L. D. Travis, "Retrieval of aerosol properties using multispectral and multiangle photopolarimetric measurements from the Research Scanning Polarimeter," Geophys. Res. Lett. **28,** 243–246 (2001).
21. J. Chowdhary, B. Cairns, and L. D. Travis, "Case studies of aerosol retrievals over the ocean from multiangle, multispectral photopolarimetric remote sensing data," J. Atmos. Sci. **59,** 383–397 (2002).
22. M. I. Sancer, "Shadow-corrected electromagnetic scattering

from a randomly-rough ocean surface," IEEE Trans. Antennas Propag. **17,** 557–585 (1969).
23. A. Morel, K. J. Voss, and B. Gentili, "Bidirectional reflectance of oceanic waters: A comparison of modeled and measured upward radiance fields," J. Geophys. Res. **100,** C7, 13,143–13,150 (1995).
24. R. W. Preisendorfer and C. D. Mobley, "Albedos and glitter patterns of a wind-roughened sea surface," J. Phys. Oceanogr. **16,** 1293–1316 (1986).
25. M. Wang and S. W. Bailey, "Correction of the sunglint contamination on the SeaWiFS aerosol optical thickness retrieval," in *SeaWiFS Postlaunch Calibration and Validation Analyses*, Part I (SeaWiFS Technical Report Series, NASA Goddard Space Flight Center, Greenbelt, Md., 2000), Chap. 9, pp. 65–69.
26. R. G. Kleidman, Y. J. Kaufman, B-C Gao, L. A. Remer, V. G. Brackett, R. A. Ferrare, E. V. Browell, and S. Ismail, "Remote sensing of total precipitable water vapor in the near-IR over ocean glint," Geophys. Res. Lett. **27,** 2657–2660 (2000).
27. Y. J. Kaufman, J. V. Martins, L. A. Remer, M. R. Schoeberl, and M. A. Yamasoe, "Retrieval of black carbon absorption from proposed satellite measurements over the ocean glint," Geophys. Res. Lett. **29,** 34-1–34-4, doi: 10.1029/2002GL015403 (2002).
28. J. Wu, "Sea-surface slope and equilibrium wind-wave spectra," Phys. Fluids **13,** 741–747 (1972).
29. E. F. Vermote, D. Tanre, J. L. Deuze, M. Herman, and J.-J. Morcrette, "Second simulation of the satellite signal in the solar spectrum, 6S: an overview," IEEE Trans. Geosci. Remote Sens. **35,** 675–686 (1997).
30. R. B. Stull, *An Introduction to Boundary Layer Meteorology* (Kluwer Academic Publishers, Dordrecht, The Netherlands, 1988), pp. 377–380.